


Self-Supervised Scalable Deep Compressed Sensing

Bin Chen¹ Xuanyu Zhang¹ Shuai Liu² Yongbing Zhang³ Jian Zhang¹ 

¹ Peking University Shenzhen Graduate School

² Shenzhen International Graduate School, Tsinghua University

³ Harbin Institute of Technology (Shenzhen)

<https://github.com/Guaishou74851/SCNet>

Abstract

Compressed sensing (CS) is a promising tool for reducing sampling costs. Current deep neural network (NN)-based CS methods face challenges in collecting labeled measurement-ground truth (GT) data and generalizing to real applications. This paper proposes a novel Self-supervised sCalable deep CS method, comprising a Learning scheme called SCL and a family of Networks named SCNet, which does not require GT and can handle arbitrary sampling ratios and matrices once trained on a partial measurement set. Our SCL contains a dual-domain loss and a four-stage recovery strategy. The former encourages a cross-consistency on two measurement parts and a sampling-reconstruction cycle-consistency regarding arbitrary ratios and matrices to maximize data/information utilization. The latter can progressively leverage common signal prior in external measurements and internal characteristics of test samples and learned NNs to improve accuracy. SCNet combines the explicit guidance from optimization algorithms with implicit regularization from advanced NN blocks to learn a collaborative signal representation. Our theoretical analyses and experiments on simulated and real captured data, covering 1-/2-/3-D natural and scientific signals, demonstrate the effectiveness, superior performance, flexibility, and generalization ability of our method over existing self-supervised methods and its significant potential in competing against state-of-the-art supervised methods.

1 Introduction

Compressed sensing (CS) [1, 2] is a pioneering paradigm that breaks through the limit of Nyquist-Shannon theorem [3] and has derived various practical applications like single-pixel imaging (SPI) [4–6], accelerated magnetic resonance imaging (MRI) [7, 8], sparse-view computational tomography (CT) [9], and snapshot compressive imaging (SCI) [10, 11]. The fundamental goal of CS imaging is to predict the high-dimensional image $\mathbf{x} \in \mathbb{R}^N$ from its low-dimensional degraded measurement $\mathbf{y} = \mathbf{A}\mathbf{x} + \mathbf{n} \in \mathbb{R}^M$, where the linear projection is achieved by a sampling matrix $\mathbf{A} \in \mathbb{R}^{M \times N}$, and $\mathbf{n} \sim q_{\mathbf{n}}$ is commonly assumed to be the additive white Gaussian noise (AWGN). In practice, extremely low values of CS ratio (or sampling rate) defined as $\gamma = M/N$ with $M \ll N$ bring not only the benefits of sampling reduction (*e.g.*, energy saving [4], acceleration [8], and suppression of X-ray radiation [9]), but also the difficulty of inferring \mathbf{x} from only \mathbf{y} and \mathbf{A} as it becomes ill-posed. Early attempts, represented by the iterative optimization algorithms [12–15], exploit image priors (*e.g.*, sparsity [16] and low-rankness [17]) to impose regularization with theoretical guarantees [18–20].

Deep neural networks (NN) achieves great success in CS over the past decade [8, 21–34]. Typically, traditional *supervised* methods fit a reconstruction NN \mathcal{F}_{Θ} with parameter set Θ to the latent target mapping $\mathbf{y} \mapsto \mathbf{x}$ by solving $\min_{\Theta} \sum_{i=1}^l \|\mathcal{F}_{\Theta}(\mathbf{y}_i) - \mathbf{x}_i\|_2^2$ on a labeled dataset $\{(\mathbf{y}_i, \mathbf{x}_i)\}$, consisting of l pairs of measurement \mathbf{y} and its ground truth (GT) \mathbf{x} . However, registered (\mathbf{y}, \mathbf{x}) pairs can be prohibitively expensive and even physically impossible to obtain in many applications like medical imaging, ghost imaging [35], biomicroscopic imaging [36], and astronomical imaging [37]. In addition, insufficient training data, domain gaps between natural and scientific images, or simulated and real measurements [38, 39], and low-quality GTs can introduce bias and overfitting to NNs, and result in their poor generalization with performance drops to real deployments of CS systems [40].

Recent progress in *unsupervised* methods provides viable solutions to alleviate data requirements. Untrained NN priors [41] leverage the implicit regularization of deep networks (*e.g.*, convolutional [42, 43] and Bayesian [44]) with early stopping and dropout [45] techniques to recover a faithful estimation from single measurement. Building on the remarkable advancements brought by Noise2Noise (N2N) [46] and Stein’s unbiased risk estimator (SURE) [47, 48]-based methods [49, 50] for image denoising, [51–53] train recovery and artifact-removal networks on measurement pairs. [54, 55] combine SURE and the learned denoising-based approximate message passing (LDAMP) [56] framework for single measurements. Equivariance constraints are introduced in [57–59] to learn components in the non-trivial nullspace of \mathbf{A} . Further advancements in signal model learning from measurements sensed by multiple operators are achieved by [60, 61], where the necessary and sufficient conditions are both presented. Inspired by the recorrputed-to-recorrputed (R2R) [62] denoising approach, [40] develops a double-head noise injection-based method and a fast adaption scheme. In [63], an adaptive stochastic gradient Langevin dynamics-based sampling is employed to approximate the Bayesian estimator of GTs. These methods break free from the dependence on large amounts of labeled data. Moreover, there is also a line of works [64–69] using generative adversarial networks (GAN) to reconstruct without requirements on (\mathbf{y}, \mathbf{x}) pairs. Some plug-and-play (PnP) [70–74], regularization by denoising (RED) [75, 76], and diffusion model [77–80]-based methods employ deep denoiser priors [81, 82] in a zero-shot manner, but they may still require GT \mathbf{x} s for modeling the clean image distribution $q_{\mathbf{x}}$.

Research Scope and Task Setting: This work investigates *self-supervised* deep CS reconstruction, where external measurements $\{\mathbf{y}_i^{train}\}$ sensed by a single fixed $\mathbf{A}^{train} \sim q_{\mathbf{A}}$ of ratio $\gamma^{train} \in (0, 1]$ can be available for offline training of NN \mathcal{F}_{Θ} [40]. Our aim is to obtain the GT estimation $\{\hat{\mathbf{x}}_i\}$ from test samples $\{\mathbf{y}_i^{test}\}$, matrix \mathbf{A}^{test} of ratio γ^{test} , and \mathcal{F}_{Θ} without access to $\mathbf{x} \sim q_{\mathbf{x}}$. We focus on image CS and its SPI applications [4–6] with orthonormalized Gaussian [83] and Bernoulli [84] matrices satisfying $\mathbf{A}\mathbf{A}^T = \mathbf{I}_M$. Our work can be extended to other settings [60] and data types [85].

Weaknesses of Existing Methods: (1) Inadequate performance. Current self-supervised methods [42–44, 51–55, 57, 58, 60, 40, 86, 63] may not compete against state-of-the-art supervised approaches [22, 87, 26, 25, 27, 29]. We attribute this fact to two factors. Firstly, their insufficient utilization of data and shared knowledge among different CS tasks leads to weak regularization and high risk of overfitting to incomplete measurements. Secondly, most approaches focus only on one part of NN architecture and learning scheme (*e.g.* loss function) designs, resulting in unbalanced developments and underfitting due to their dated components and training techniques. A comprehensive guidance from advanced NN frameworks like neural representation [88, 82, 89, 90], algorithm-unrolling [91–93], and its augmentations [25, 94–97] can alleviate this challenge. (2) Lack of flexibility and scalability. Most existing self-supervised CS methods [42, 44, 51, 57, 58, 60, 40, 63] treat different matrices or ratios as independent tasks, requiring measurement re-samplings, re-trainings, or lengthy adaptations to adjust models to new imaging devices or reconstruction quality levels. The increase in samplings, model number, and training time has detrimental effects on the object being captured (*e.g.* human body) and consumes considerable storage and computational resources, making them impractical for embedded and mobile deployments [24]. For instance, in wireless broadcast [98, 99], terminal users can receive images of different ratios based on their channel conditions. In medical and biomicroscopic imaging, additional measurements can be acquired to enhance tissue and cell details. However, suppose there are d systems equipped with d complete matrices, current methods [51, 57, 58, 60, 40] need up to dN^1 dataset constructions, NN trainings, or adaptations to address all possible requirements. Thus, ratio-scalable and matrix-adaptive reconstruction [100, 24, 29, 101, 31] is actually preferred for real applications, which is not adequately addressed by existing self-supervised deep CS methods.

This paper proposes a Self-supervised sCalable deep CS method, consisting of a Learning scheme named **SCL** and a Network family called **SCNet**. Inspired by the success of N2N [46] and controllable NNs [102–105, 27, 29, 31, 81, 106], SCL imposes a cross-supervision mechanism [52] between two divided parts of each CS measurement with random lengths and a cycle-consistency constraint on sampling-reconstruction pipeline regarding arbitrary ratios/matrices [29] to improve task diversity and NN robustness. SCNet combines the concepts of algorithm-unrolling [92] and implicit neural representation [82] to develop a new recovery NN that achieves a better trade-off among performance, flexibility, scalability, complexity, and interpretability compared to existing approaches. Our method supports arbitrary scenarios $\mathbf{x} \sim q_{\mathbf{x}}$, CS ratios $\gamma \in (0, 1]$, and matrices $\mathbf{A} \sim q_{\mathbf{A}}$ once trained on the measurement set of a single matrix with fixed ratio (*e.g.* 10%), and can flexibly adapt to test samples

¹There are at most N discrete CS ratios in practice, *i.e.*, $\gamma \in \{1/N, 2/N, \dots, N/N\}$. In our experiments, d and N can reach 2 and 1089 (or 16384), respectively. They can be even much larger in real applications.

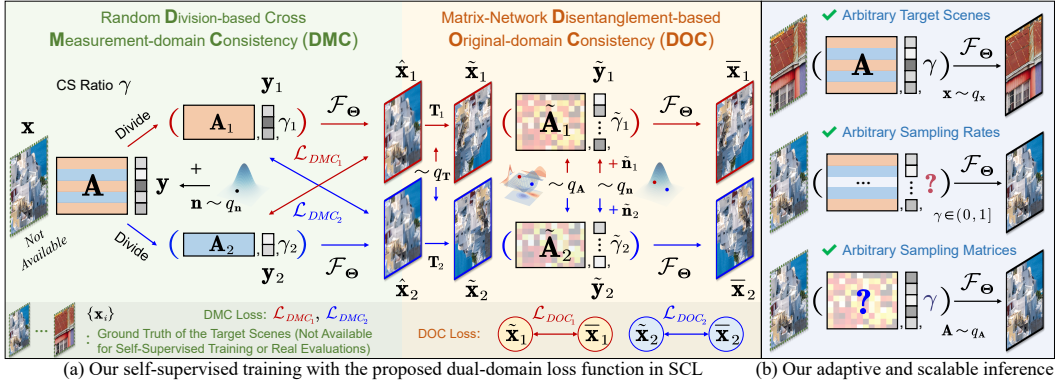


Figure 1: Illustration of our self-supervised dual-domain loss. (a) We encourage DMC and DOC for any matrices/ratios/noises, aiming to learn common priors of latent signals and entire CS domain without overfitting to specific ones. (b) Once the recovery NN is learned, it can generalize to arbitrary in-distribution scenes/ratios/matrices not seen in the training set, to support changeable requirements.

for further improvements if needed. By resolving the two limitations (1)-(2), it paves a practical way for high-quality and scalable CS for data-limited and requirement-changeable real environments.

Contributions: (1) A self-supervised CS learning scheme named SCL, which includes a dual-domain loss and a four-stage progressive reconstruction strategy. (2) An NN family dubbed SCNet, which combines explicit guidance from traditional proximal gradient descent (PGD) algorithm [107] and implicit regularization from advanced NN components. (3) Extensive experiments conducted on simulated and real data of 1D, 2D, and 3D signals exhibit the significant superiority and effectiveness of our method in improving both recovery quality and generalization ability. A real SPI optics system is established for performance validation on fluorescence microscopy [108]. Corresponding analyses and discussions are also provided to try to offer an understanding of our method’s working principle.

2 Proposed Method

This section introduces our SCL and SCNet. Sec. 2.1 presents SCL, comprising a dual-domain loss and a four-stage recovery strategy. The former includes a Division-based cross Measurement-domain Consistency (DMC) constraint, which is improved from the loss equivalent in terms of expectation bounds to the noise-free supervised loss under certain conditions, and maximized fine-grained data augmentation (by up to $\sim 2^M \times$ expansion in the size of measurement set), as well as a matrix-network Disentanglement-based Original-domain Consistency (DOC) constraint, that leverages the available information of distributions q_x , q_n , and q_A to impose consistency on the sampling-reconstruction cycle. The latter first learns the common signal prior among external measurements and then exploits the internal statistics of test samples in a coarse-to-fine manner. Sec. 2.2 presents SCNet, a family of simple yet efficient recovery NNs that can work synergistically and achieve mutual support with SCL.

2.1 Self-Supervised Scalable Reconstruction Learning (SCL)

(1) Dual-Domain Loss Function. Given NN structure \mathcal{F}_Θ , measurement y , matrix A , and ratio γ , a widely adopted and straightforward practice of self-supervised CS recovery is to enforce the measurement consistency (MC) on \mathcal{F}_Θ using a loss of form like $\mathcal{L}_{MC} = \|A\hat{x} - y\|_2^2$ with $\hat{x} = \mathcal{F}_\Theta(y)$, which, however, easily brings overfitting to inharmonious results, faced with two critical problems [44, 58, 40]: (1) **The presence of noise.** n is not suppressed and can propagate from y to \hat{x} . (2) **The solution ambiguity.** \hat{x} converges freely to $A^\dagger y + \mathcal{H}(y)$ satisfying $A\hat{x} = AA^\dagger y + A\mathcal{H}(y) = y$ with $\mathcal{H}(y) \in \text{null}(A)$, where A^\dagger is the right pseudo-inverse of A and $\text{null}(A) = \{w \in \mathbb{R}^N | Aw = 0_M\}$ is the $(N - M)$ -dimensional nullspace of A . This causes unstable outputs without meeting $\hat{x} = x$.

To mitigate these issues and make \mathcal{F}_Θ adaptive to the changes of CS ratio and matrix, we develop a new division-based measurement-domain consistency (DMC) loss, which employs the combinations of measurement elements from y to construct thousands of new tasks with different matrices and ratios for augmentation on data diversity. As illustrated in Fig. 1 (a, left), we randomly divide the original task (y, A, γ) into two complementary parts (y_1, A_1, γ_1) and (y_2, A_2, γ_2) satisfying the conditions of $S_{y_1} \cup S_{y_2} = S_y$, $S_{A_1} \cup S_{A_2} = S_A$, $S_{y_1} \cap S_{y_2} = S_{A_1} \cap S_{A_2} = \emptyset$, and $\gamma_1 + \gamma_2 = \gamma$. Here, $S_y = \{(i, y[i])\}_{i=1}^M$ and $S_A = \{(i, A[i])\}_{i=1}^M$ are the set representations of y and A . $y[i]$ and $A[i]$ denote the measurement element and matrix row at index i , while M_1 and M_2 represent the dimensions of y_1 and y_2 with $M_1 + M_2 = M$, respectively. Our goal is to reconstruct $\hat{x}_1 = \mathcal{F}_\Theta(y_1, A_1, \gamma_1)$ that takes matrix and ratio as conditional inputs and can conform to the following two constraints:

$$\text{Self-MC Constraint: } \mathbf{A}_1 \hat{\mathbf{x}}_1 = \mathbf{A}_1 \mathbf{x}, \quad (1) \quad \text{Cross-MC Constraint: } \mathbf{A}_2 \hat{\mathbf{x}}_1 = \mathbf{A}_2 \mathbf{x}. \quad (2)$$

While Eq. (1) can be partially addressed by a self-loss $\mathcal{L}_{self_1} = \|\mathbf{A}_1 \hat{\mathbf{x}}_1 - \mathbf{y}_1\|_2^2$ [51] and SURE-based loss [58], we focus on the encouragement of Eq. (2) by $\mathcal{L}_{cross_1} = \|\mathbf{A}_2 \hat{\mathbf{x}}_1 - \mathbf{y}_2\|_2^2$, which is naturally noise-resistant and tightly connected to its supervised counterpart with two assumptions as follows:

Assumption 1 (Distribution of the observation noise). *The noise \mathbf{n} is AWGN with zero mean and standard deviation (or noise level) σ , i.e., $\mathbf{n} \sim q_{\mathbf{n}} = \mathcal{N}(\mathbf{0}_M, \sigma^2 \mathbf{I}_M)$. The noise components \mathbf{n}_1 and \mathbf{n}_2 in the divided measurements $\mathbf{y}_1 = \mathbf{A}_1 \mathbf{x} + \mathbf{n}_1$ and $\mathbf{y}_2 = \mathbf{A}_2 \mathbf{x} + \mathbf{n}_2$ are mutually independent.*

Assumption 2 (Properties of images and sampling matrices) [109–112]. *The reconstructions from \mathcal{F}_{Θ} and GT \mathbf{x} are compressible s -sparse signals under a common basis Ψ with large s . The sampling matrices \mathbf{A} , \mathbf{A}_1 , and \mathbf{A}_2 are incoherent to Ψ and satisfy the restricted isometry property (RIP) [110] of order $2s$ with small constant $\delta \in (0, 1)$, i.e., for any $(2s)$ -sparse signal $\mathbf{v} \in \mathbb{R}^N$, there holds that:*

$$\forall \Phi \in \{\mathbf{A}, \mathbf{A}_1, \mathbf{A}_2\}, \quad (1 - \delta) \|\mathbf{v}\|_2^2 \leq \|\Phi \mathbf{v}\|_2^2 \leq (1 + \delta) \|\mathbf{v}\|_2^2.$$

Based on the above assumptions, we show important properties of \mathcal{L}_{cross_1} by the following theorems:

Theorem 1 (Equivalence of cross-MC loss to its noise-free counterpart). *The cross-MC loss is equivalent in terms of expectation to the noise-free one for encouraging Eq. (2), i.e., there holds that:*

$$J = \mathbb{E}_{\mathbf{y}_1, \mathbf{y}_2} \{\|\mathbf{A}_2 \mathcal{F}_{\Theta}(\mathbf{y}_1, \mathbf{A}_1, \gamma_1) - \mathbf{y}_2\|_2^2\} = \mathbb{E}_{\mathbf{x}, \mathbf{n}_1} \{\|\mathbf{A}_2 [\mathcal{F}_{\Theta}(\mathbf{A}_1 \mathbf{x} + \mathbf{n}_1, \mathbf{A}_1, \gamma_1) - \mathbf{x}]\|_2^2\} + M_2 \sigma^2$$

Proof. Please refer to Sec. D.1 in the [supplementary material](#) for our proof and more details. ■

Theorem 2 (Boundness of the supervised loss via cross-MC loss). *The supervised loss $\mathcal{L}_{sup_1} = \|\hat{\mathbf{x}}_1 - \mathbf{x}\|_2^2$ is bounded in terms of expectation by $(\mathcal{L}_{cross_1} - M_2 \sigma^2)$ and $\frac{\mathcal{L}_{cross_1} - M_2 \sigma^2}{1 - \delta}$, i.e., there is:*

$$J - M_2 \sigma^2 \leq \mathbb{E}_{\mathbf{x}, \mathbf{n}_1} \{\|\mathcal{F}_{\Theta}(\mathbf{A}_1 \mathbf{x} + \mathbf{n}_1, \mathbf{A}_1, \gamma_1) - \mathbf{x}\|_2^2\} \leq \frac{J - M_2 \sigma^2}{1 - \delta}$$

Proof. Please refer to Sec. D.2 in the [supplementary material](#) for our proof and more details. ■

Note that the RIP condition of **Assum. 2** utilized in **Thm. 2** can be satisfied with high probability for sparse natural signals under some certain conditions [110]. Our provided **Thms. 1** and **2** indicate that \mathcal{L}_{cross_1} can be the unbiased estimators and lower/upper bounds of the supervised losses, thus revealing its effectiveness for self-supervision. Here we also propose to generalize the ℓ_2 error form in \mathcal{L}_{cross_1} from $\|\cdot\|_2^2$ to the ℓ_p form $\|\cdot\|_p^p$ and set $p = 1$ by default. The reason is that the original ℓ_2 loss can lead to undesirable biased learning of \mathcal{F}_{Θ} toward low-ratio tasks, since their loss values may become almost three orders of magnitude larger than those of high-ratio ones due to their less input information and higher recovery difficulty, while our ℓ_p loss can significantly alleviate this issue in practice. A loss term $\|\mathbf{A}_1 \hat{\mathbf{x}}_2 - \mathbf{y}_1\|_p^p$ symmetric to \mathcal{L}_{cross_1} with $\hat{\mathbf{x}}_2 = \mathcal{F}_{\Theta}(\mathbf{y}_2, \mathbf{A}_2, \gamma_2)$ is introduced to make ratios balanced and data utilization adequate, thus improving final performance. We do not enforce the self-MC in Eq. (1) as we observe that the cross-MC encouragement in Eq. (2) is dominant and competent for assurance of reconstruction accuracy. To summarize, our DMC loss is defined as:

$$\mathcal{L}_{DMC} = \mathcal{L}_{DMC_1} + \mathcal{L}_{DMC_2}, \quad \mathcal{L}_{DMC_1} = \|\mathbf{A}_2 \hat{\mathbf{x}}_1 - \mathbf{y}_2\|_p^p, \quad \mathcal{L}_{DMC_2} = \|\mathbf{A}_1 \hat{\mathbf{x}}_2 - \mathbf{y}_1\|_p^p. \quad (3)$$

To liberate \mathcal{F}_{Θ} from the dependence on specific internal information of $(\mathbf{y}, \mathbf{A}, \gamma)$ instances and enable its learning beyond \mathbf{y} , \mathbf{A} and ratio range $(0, \gamma]$, while generalizing across the entire matrix space and range $(0, 1]$, we introduce a new matrix-network disentanglement-based original-domain consistency (DOC) loss. As Fig. 1 (a, right) shows, it leverages estimation $\tilde{\mathbf{x}}$ from \mathcal{L}_{DMC} calculation and jointly exploits the information of $q_{\mathbf{x}}$, $q_{\mathbf{n}}$, and $q_{\mathbf{A}}$ to establish a connection between measurement and original domains, enforcing a cycle-consistency of sampling-reconstruction for arbitrary in-distribution tasks:

$$\text{DOC Constraint: } \forall \mathbf{T}, \forall \tilde{\mathbf{A}}, \forall \tilde{\mathbf{n}}, \forall \tilde{M} \in \{1, \dots, N\}, \quad \bar{\mathbf{x}} = \mathcal{F}_{\Theta}(\tilde{\mathbf{y}}, \tilde{\mathbf{A}}, \tilde{\gamma}) = \tilde{\mathbf{x}}. \quad (4)$$

Here, $\tilde{\mathbf{y}} = \tilde{\mathbf{A}} \tilde{\mathbf{x}} + \tilde{\mathbf{n}}$ represents a new simulated observation, $\tilde{\mathbf{x}} = \mathbf{T} \hat{\mathbf{x}}$ is a diversity-augmented version of $\hat{\mathbf{x}}$ using a geometric transformation matrix $\mathbf{T} \in \mathbb{R}^{N \times N}$ [59], while the ratio is given by $\tilde{\gamma} = \tilde{M}/N$. Based on Eq. (4), our DOC loss is defined as a sum of two terms for both the estimations $\hat{\mathbf{x}}_1$ and $\hat{\mathbf{x}}_2$:

$$\mathcal{L}_{DOC} = \mathcal{L}_{DOC_1} + \mathcal{L}_{DOC_2}, \quad \mathcal{L}_{DOC_1} = \|\bar{\mathbf{x}}_1 - \tilde{\mathbf{x}}_1\|_p^p, \quad \mathcal{L}_{DOC_2} = \|\bar{\mathbf{x}}_2 - \tilde{\mathbf{x}}_2\|_p^p, \quad (5)$$

$$\forall i \in \{1, 2\}, \quad \bar{\mathbf{x}}_i = \mathcal{F}_{\Theta}(\tilde{\mathbf{y}}_i, \tilde{\mathbf{A}}_i, \tilde{\gamma}_i), \quad \tilde{\mathbf{y}}_i = \tilde{\mathbf{A}}_i \tilde{\mathbf{x}}_i + \tilde{\mathbf{n}}_i, \quad \tilde{\mathbf{x}}_i = \mathbf{T}_i \hat{\mathbf{x}}_i, \quad \tilde{\gamma}_i = \tilde{M}_i/N.$$

For each estimation $\hat{\mathbf{x}}_i$ in the training batch, $\mathbf{T}_i \sim q_{\mathbf{T}}$ is first randomly drawn from eight classic group actions on the natural image set [57, 58], including rotations, flippings, and their combinations [31]. $\tilde{M}_i \sim \text{Uniform}(\{1, \dots, N\})$, $\tilde{\mathbf{A}}_i \sim q_{\mathbf{A}}$, and $\tilde{\mathbf{n}}_i \sim q_{\mathbf{n}}$ are then sampled to create CS task $(\tilde{\mathbf{y}}_i, \tilde{\mathbf{A}}_i, \tilde{\gamma}_i)$ for DOC encouragement². Finally, we combine the two loss parts \mathcal{L}_{DMC} and \mathcal{L}_{DOC} in Eqs. (3) and (5) using a weighting factor α to obtain our dual-domain self-supervised loss $\mathcal{L} = \mathcal{L}_{DMC} + \alpha \mathcal{L}_{DOC}$.

(2) Four-Stage Progressive Reconstruction Strategy. As Fig. 1 (b) exhibits, our \mathcal{L} learns common signal priors from external measurements in an offline manner [86], making \mathcal{F}_{Θ} adaptive for arbitrary CS tasks once trained. Nevertheless, the success of dataset-free approaches [42, 44, 63] demonstrates the potential of fitting NN weights to specific test \mathbf{y} samples, enabling an online reconstruction and further improvement. Based on insights in [10, 34, 40], we design a strategy that takes advantage of the GT-free nature of \mathcal{L} for both training and test to alleviate the risks posed by external data bias and out-of-distribution \mathbf{y} samples, and further enhance final performance. It consists of four stages as:

(Stage-1) Training-time offline external learning:	Fit \mathcal{F}_{Θ} on $\{\mathbf{y}_i^{train}\}$ of size l^{train} and \mathbf{A}^{train} by our \mathcal{L}
(Stage-2) Test-time cross-image internal learning:	Fit \mathcal{F}_{Θ} on $\{\mathbf{y}_i^{test}\}$ of size l^{test} and \mathbf{A}^{test} by our \mathcal{L}
(Stage-3) Test-time single-image internal learning:	Fit \mathcal{F}_{Θ} on the specific task $(\mathbf{y}^{test}, \mathbf{A}^{test}, \gamma^{test})$ by our \mathcal{L}
(Stage-4) Test-time single-image self-ensemble:	Generate estimation by $\hat{\mathbf{x}}^* = \mathbb{E}_{\mathbf{M}, \mathbf{T}} \{\mathbf{T}^{-1} \mathcal{F}_{\Theta}(\mathbf{y}, \mathbf{M} \mathbf{A} \mathbf{T}, \gamma)\}$

Considering that measurements in a single test set can share common knowledge of the same scene, such as similar structures and textures contained in their latent GTs, our test-time internal learning (stages 2 and 3) first fits \mathcal{F}_{Θ} to the entire test set and then adapts it to each specific measurement in a coarse-to-fine manner. To further exploit the generalization ability of \mathcal{F}_{Θ} to arbitrary matrices, we propose a self-ensemble inference in stage-4, which averages D recovered images from \mathcal{F}_{Θ} with D randomly perturbed \mathbf{A} inputs to approximate the final estimation $\hat{\mathbf{x}}^*$ via Monte Carlo sampling [113]:

$$\text{Self-Ensemble: } \hat{\mathbf{x}}^* = \mathbb{E}_{\mathbf{M}, \mathbf{T}} \{\mathbf{T}^{-1} \mathcal{F}_{\Theta}(\mathbf{y}, \mathbf{M} \mathbf{A} \mathbf{T}, \gamma)\} \approx \frac{1}{D} \sum_{i=1}^D \mathbf{T}_i^{-1} \mathcal{F}_{\Theta}(\mathbf{y}, \mathbf{M}_i \mathbf{A} \mathbf{T}_i, \gamma), \quad (6)$$

where $\mathbf{M} \in \{0, 1\}^{M \times M}$ is a diagonal matrix whose elements have a probability of r for being 0 and $(1 - r)$ for being 1. This self-ensemble stems from our observation that the geometric transformations in \mathcal{L}_{DOC} and random maskings on \mathbf{A} with a small r can preserve the low-frequency smooth image components with high confidence, and generate predictions for high-frequency textures, which exhibit certain degree of independence and can be averaged to suppress artifacts and yield better results [86]. It closely relates to our unrolled NN design that is described in Sec. 2.2. In practice, customizations on the strategy can be flexibly implemented based on specific requirements, like the fully-activated one denoted by $(1 \rightarrow 2 \rightarrow 3 \rightarrow 4)$ for best performance, $(1 \rightarrow 4)$ for training resource-constrained devices, and $(3 \rightarrow 4)$ for dataset-free deployments. Parameters Θ are randomly initialized for the first stage of each configuration and saved to the next ones once learning completed stage-by-stage.

2.2 Collaborative Representation-based Reconstruction Network (SCNet)

CS recovery from $(\mathbf{y}, \mathbf{A}, \gamma)$ can be formulated as a regularized optimization problem: $\min_{\mathbf{x}} \frac{1}{2} \|\mathbf{A}\mathbf{x} - \mathbf{y}\|_2^2 + \lambda \mathcal{R}(\mathbf{x})$, which can be solved by the proximal gradient descent (PGD) algorithm [107] as:

$$\text{Gradient Descent (GD): } \mathbf{z}^{(k)} = \hat{\mathbf{x}}^{(k-1)} - \rho \mathbf{A}^{\top} (\mathbf{A} \hat{\mathbf{x}}^{(k-1)} - \mathbf{y}) \in \mathbb{R}^N, \quad (7)$$

$$\text{Proximal Mapping (PM): } \hat{\mathbf{x}}^{(k)} = \text{prox}_{\lambda \mathcal{R}}(\mathbf{z}^{(k)}) = \arg \min_{\mathbf{x}} \frac{1}{2} \|\mathbf{x} - \mathbf{z}^{(k)}\|_2^2 + \lambda \mathcal{R}(\mathbf{x}) \in \mathbb{R}^N, \quad (8)$$

where k and ρ denote the iteration index and step size, respectively. Following [91, 92] and their augmentations [93–97], we develop SCNet to implement \mathcal{F}_{Θ} that is inspired by PGD and can adapt to different tasks once trained with SCL. As Fig. 2 shows, its recovery consists of three sub-processes:

(1) Shallow Feature Initialization. The measurement \mathbf{y} is first transformed to the image domain by $\mathbf{A}^{\dagger} \mathbf{y}$ and concatenated with a CS ratio map \mathbf{R} , which has the same shape as $\mathbf{x} \in \mathbb{R}^{1 \times H \times W}$ with all elements being γ . The shallow feature of our data concatenation $[\mathbf{A}^{\dagger} \mathbf{y}, \mathbf{R}] \in \mathbb{R}^{2 \times H \times W}$ is then extracted by a convolution layer \mathcal{F}_{ext} for initialization as $\hat{\mathbf{X}}^{init} = \mathcal{F}_{ext}([\mathbf{A}^{\dagger} \mathbf{y}, \mathbf{R}]) \in \mathbb{R}^{C \times H \times W}$.

(2) Deep Feature Refinement. We extend the PGD unrolling [92] from the traditional image-level optimization to a high-throughput feature-level recovery with a maximized information flow [93]. Specifically, given an initial starting feature $\hat{\mathbf{X}}^{(0)} \in \mathbb{R}^{C \times H \times W}$, we generalize the original PGD steps

²In this paper, we may not strictly distinguish distributions of different data dimensions corresponding to the same data type (e.g., noise) using separate notations (e.g., $q_{\mathbf{n}, \tilde{M}_1}$ and $q_{\mathbf{n}, \tilde{M}_2}$) for conciseness without confusion.

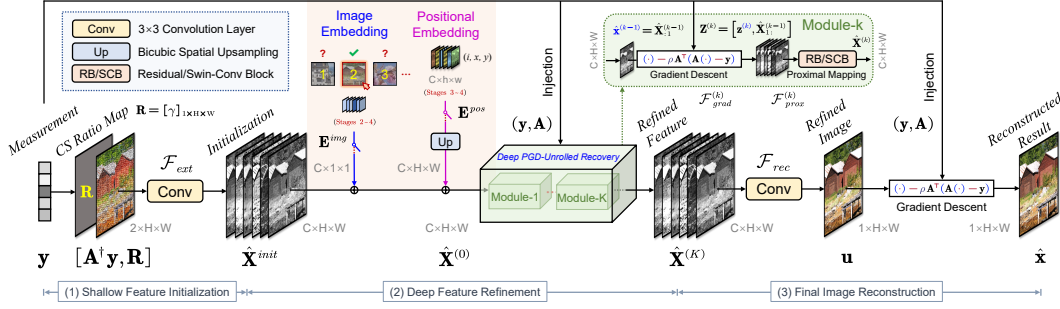


Figure 2: Illustration of SCNet, which extracts a shallow feature, injects two embeddings, and refines by unrolled modules. It combines explicit guidance of PGD and implicit regularization of NN blocks, yielding a collaborative representation. Final result is obtained by a convolution with a GD update.

in Eqs. (7) and (8) to their feature-level unrolling extensions, denoted by $\mathcal{F}_{grad}^{(k)}$ and $\mathcal{F}_{prox}^{(k)}$, as follows:

$$\text{Generalized GD from (7): } \mathbf{Z}^{(k)} = \mathcal{F}_{grad}^{(k)}(\hat{\mathbf{X}}^{(k-1)}; \mathbf{y}, \mathbf{A}) = [\mathbf{z}^{(k)}, \hat{\mathbf{X}}_{1:}^{(k-1)}] \in \mathbb{R}^{C \times H \times W}, \quad (9)$$

$$\text{Generalized PM from (8): } \hat{\mathbf{X}}^{(k)} = \mathcal{F}_{prox}^{(k)}(\mathbf{Z}^{(k)}) \in \mathbb{R}^{C \times H \times W} \quad (\mathcal{F}_{prox}^{(k)} \text{ is an RB or SCB}). \quad (10)$$

Here, $\mathbf{Z}^{(k)}$ is obtained by analytically updating only the first channel of $\hat{\mathbf{X}}^{(k-1)}$ using Eq. (7) with $\hat{\mathbf{x}}^{(k-1)} = \hat{\mathbf{X}}_{1:}^{(k-1)}$, while leaving the other feature channels $\hat{\mathbf{X}}_{1:}^{(k-1)}$ unchanged. The second update step of $\hat{\mathbf{X}}^{(k)}$ is implemented by a single residual block (RB) [114] for the convolutional SCNet version called **SC-CNN**, or an advanced Swin-Conv block (SCB) [115] for the Transformer-based SCNet version named **SCT**. We unroll a total of K generalized PGD iterations with each one converted into an NN module that sequentially conducts the two steps in Eqs. (9) and (10). While most NN blocks are generally treated as “black-box” components, we present a theoretical conclusion that reveals the effectiveness, feasibility, and potential of GD steps in Eqs. (7) and (9) for performance improvement:

Theorem 3 (Potential of the GD step for Reducing Prediction Error). *Given any estimation $\hat{\mathbf{x}}$ of GT \mathbf{x} satisfying $\|\hat{\mathbf{x}} - \mathbf{x}\|_2^2 < \infty$, the GD step performed on $\hat{\mathbf{x}}$ yielding \mathbf{z} can reduce the error expectation from $e_{\hat{\mathbf{x}}} = \mathbb{E}_{\mathbf{n}} \{\|\hat{\mathbf{x}} - \mathbf{x}\|_2^2\}$ to $e_{\mathbf{z}} = \mathbb{E}_{\mathbf{n}} \{\|\mathbf{z} - \mathbf{x}\|_2^2\}$ with a margin $\Delta e = e_{\hat{\mathbf{x}}} - e_{\mathbf{z}}$ by appropriate step sizes ρ . For any $\sigma \in [0, +\infty)$, there exists a “best” step size $\rho^* = 1 - \frac{M\sigma^2}{M\sigma^2 + \mathbb{E}_{\mathbf{n}} \{\|\mathbf{A}(\hat{\mathbf{x}} - \mathbf{x})\|_2^2\}} \in (0, 1]$ that leads to minimal error expectation $e_{\mathbf{z}}^* = e_{\hat{\mathbf{x}}} - (\Delta e)^*$ with maximal error reduction $(\Delta e)^* = \rho^* \mathbb{E}_{\mathbf{n}} \{\|\mathbf{A}(\hat{\mathbf{x}} - \mathbf{x})\|_2^2\}$. When $\rho \in [0, 2\rho^*]$, there holds that $\Delta e = e_{\hat{\mathbf{x}}} - e_{\mathbf{z}} \geq 0$. The ratio of minimal error expectation to the original one is bounded as $1 \geq (e_{\mathbf{z}}^*/e_{\hat{\mathbf{x}}}) \in [1 - \rho^*(1 + \delta), 1 - \rho^*(1 - \delta)]$.*

Proof. Please refer to Sec. D.3 in the [supplementary material](#) for our proof and more details. ■

Our **Thm. 3** suggests that the GD steps can improve reconstructions with appropriate step sizes. To avoid the non-trivial processes of finding or estimating optimal ρ s, while still maintaining simplicity and efficacy, we set $\rho \equiv 1$ for $\sigma = 0$ cases and re-parameterize it as $\rho = \text{Sigmoid}(\tau)$ to make it data-driven and limited in range $(0, 1]$ with a learnable parameter τ for $\sigma > 0$ cases. We have observed that these straightforward ρ settings can be competent for facilitating our “SCL+SCNet” training. To enhance flexibility and balance between performance and interpretability, SCNet not only constrains results by explicit PGD framework and implicit priors of locality and translation invariance brought by convolutions, RBs, and SCBs, but also introduces two learnable embeddings to increase optimization freedom and prevent underfitting. The first is an image embedding (IE) $\mathbf{E}^{img} \in \mathbb{R}^{C \times 1 \times 1}$ activated only for stages 2-4 and generated for each test image to help \mathcal{F}_{Θ} distinguish each specific one from the entire test set. The second is a positional embedding (PE) $\mathbf{E}^{pos} \in \mathbb{R}^{C \times h \times w}$ activated only for stages 3-4 and first upscaled using bicubic interpolation to match the feature size. It can have various values for different areas and make \mathcal{F}_{Θ} position-aware and spatially-variant. Both \mathbf{E}^{img} and \mathbf{E}^{pos} are zero-initialized and added to $\hat{\mathbf{X}}^{init}$ channel-/element-wise to generate $\hat{\mathbf{X}}^{(0)}$ before PGD-unrolled recovery. The output is the iteratively refined feature $\hat{\mathbf{X}}^{(K)}$ from the K -th deep unrolled module.

(3) Final Image Reconstruction. A refined image is first generated by $\mathbf{u} = \mathcal{F}_{rec}(\hat{\mathbf{X}}^{(K)}) \in \mathbb{R}^{1 \times H \times W}$ using a convolution layer \mathcal{F}_{rec} . The final result is then obtained by an extra GD step like Eq. (7) as:

$$\text{Final GD: } \hat{\mathbf{x}} = \mathbf{u} - \rho \mathbf{A}^T (\mathbf{A} \mathbf{u} - \mathbf{y}) = \rho \mathbf{A}^T \mathbf{y} + (\mathbf{I}_N - \rho \mathbf{A}^T \mathbf{A}) \mathbf{u} \in \mathbb{R}^N \quad (\text{with } \mathbf{A}^T = \mathbf{A}^\dagger). \quad (11)$$

It should be noted that when $\sigma = 0$, our setting $\rho \equiv 1$ ensures that $\hat{\mathbf{x}}$ strictly conforms to the self-MC in Eq. (1), i.e., $\mathbf{A} \hat{\mathbf{x}} = \mathbf{y} = \mathbf{A} \mathbf{x}$, with self-loss always being zero if calculated. In the presence of noise

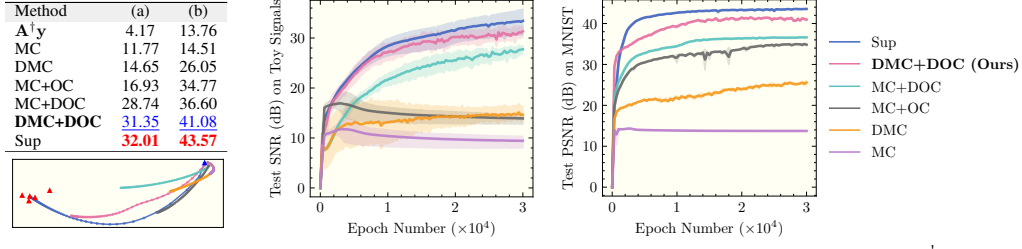


Figure 3: Comparisons of CS reconstruction for toy signals and MNIST [118] among $\mathbf{A}^\dagger \mathbf{y}$ and six SC-CNNs with scheme names/loss functions in quotes/brackets: “MC” (\mathcal{L}_{MC}), “DMC” (\mathcal{L}_{DMC}), “MC+OC” ($\mathcal{L}_{MC} + \alpha \mathcal{L}_{OC}$), “MC+DOC” ($\mathcal{L}_{MC} + \alpha \mathcal{L}_{DOC}$), our “DMC+DOC” ($\mathcal{L}_{DMC} + \alpha \mathcal{L}_{DOC}$), and “Sup” (\mathcal{L}_{sup}). (Top-left) Highest test signal-to-noise ratio (SNR, dB) on toy signals (a) and peak SNR (PSNR, dB) on MNIST (b) with ratio 50%. (Bottom-left) Optimization trajectories of NNs for MNIST, visualized by projecting weights to a 2D space with PCA [119]. Blue and red triangles represent initial and final weights optimized by \mathcal{L}_{sup} for ratio 50%, and fine-tuned results for 10%, 20%, 30%, and 40%. (Middle/Right) Test SNR/PSNR curves on toy signals/MNIST with ratio 50%.

Table 1: Comparison of average PSNR (dB) on four natural image benchmarks [22, 120–122]. The best and second-best results of each case are highlighted in bold red and underlined blue, respectively.

Method	Test Set	Set11 [22]			CBSD68 [120]			Urban100 [121]			DIV2K [122]		
	CS Ratio γ ($\sigma = 0$)	10%	30%	50%	10%	30%	50%	10%	30%	50%	10%	30%	50%
Supervised Methods	ReconNet (CVPR 2016) [22]	24.08	29.46	32.76	23.92	27.97	30.79	20.71	25.15	28.15	24.41	29.09	32.15
	ISTA-Net+ (CVPR 2018) [87]	26.49	33.70	38.07	25.14	30.24	33.94	22.81	29.83	34.33	26.30	32.65	36.88
	DPA-Net (TIP 2020) [26]	27.66	33.60	-	25.33	29.58	-	24.00	29.04	-	27.09	32.37	-
	MAC-Net (ECCV 2020) [25]	27.92	33.87	37.76	25.70	30.10	33.37	23.71	29.03	33.10	26.72	32.23	35.40
	ISTA-Net++ (ICME 2021) [27]	28.34	34.86	38.73	26.25	31.10	34.85	24.95	31.50	35.58	27.82	33.74	37.78
	COAST (TIP 2021) [29]	28.78	35.10	38.90	26.28	31.08	34.72	25.32	31.90	35.89	27.98	33.85	37.87
Self-Supervised Methods	DIP (CVPR 2018) [42]	26.09	32.58	35.30	24.73	28.47	31.81	23.37	28.23	33.15	25.42	31.32	35.03
	BCNN (CVPR 2018) [44]	27.58	33.70	37.44	25.15	29.56	33.04	24.87	31.07	35.03	26.93	32.53	36.33
	EI (ICCV 2021) [57]	21.76	33.49	37.66	22.43	29.74	33.43	19.04	28.82	33.72	22.60	32.24	36.88
	ASGLD (CVPR 2022) [63]	27.81	34.17	37.46	25.23	29.58	32.37	24.54	31.09	34.91	27.01	32.67	36.14
	DDSL (ECCV 2022) [40]	27.65	34.21	38.40	26.17	31.03	34.65	25.12	32.59	36.44	27.55	33.81	37.52
	SC-CNN (Ours)	27.93	34.95	39.07	25.81	31.03	34.84	23.75	31.52	36.13	27.33	33.86	38.13
	SC-CNN+ (Ours)	29.42	36.12	40.16	26.27	31.51	35.38	27.73	34.56	38.47	28.47	34.77	39.01
	SCT (Ours)	28.21	35.32	39.50	25.99	31.20	35.06	24.04	31.80	36.54	27.51	34.03	38.39
	SCT+ (Ours)	29.32	36.10	40.41	26.17	31.60	35.52	27.74	34.58	38.55	28.52	34.89	39.24

($\sigma > 0$), the measurement of $\hat{\mathbf{x}}$ becomes a weighted sum given by $\mathbf{A}\hat{\mathbf{x}} = \rho \mathbf{y} + (1 - \rho) \mathbf{A} \mathbf{u} \in \mathbb{R}^M$, while the nullspace component [116] of $\hat{\mathbf{x}}$ will remain the same as that of \mathbf{u} , i.e., $(\mathbf{I}_N - \mathbf{A}^\dagger \mathbf{A}) \hat{\mathbf{x}} = (\mathbf{I}_N - \mathbf{A}^\dagger \mathbf{A}) \mathbf{u} \in \mathbb{R}^N$. This final GD step is motivated by the success of residual learning [117] for measurement denoising and has been demonstrated to be effective in facilitating our SCL training.

Formally, all the learnable parameters of our SCNet can be expressed as the set $\Theta = \{\mathcal{F}_{ext}, \mathcal{F}_{rec}, \tau\} \cup \{\mathbf{E}_i^{img}, \mathbf{E}_i^{pos}\}_{i=1}^{l^{test}} \cup \{\mathcal{F}_{prox}^{(k)}\}_{k=1}^K$, where l^{test} is the size of test set. Each unrolled module of SCNet has its own parameters in $\mathcal{F}_{prox}^{(k)}$ implemented by an RB or SCB for SC-CNN or SCT. We define the SCNets trained by stage-1 only as the standard versions, while their enhanced ones are obtained by incorporating the complete SCL process of stages 1-4, denoted as **SC-CNN+** and **SCT+**, respectively.

3 Experiments³

In this section, we present evaluations of our method on four different types of data: (1) synthesized toy signals, (2) handwritten digit images from the MNIST dataset, (3) natural images, and (4) real captured measurements for SPI. All the experiments are conducted on an NVIDIA RTX 4090 GPU.

3.1 CS Reconstruction for Toy Signals and MNIST Digit Images

Setup. We first study the efficacy of our method on 1D 2-sparse toy signals and the MNIST [118] dataset. The toy signals are generated by $\mathbf{x} = \Psi \mathbf{s}$ of size 32, where Ψ denotes the DCT basis and \mathbf{s} has its first 2 elements being sampled from a joint distribution, with the other 30 being zero. We employ 4 bivariate toy distributions [37], including a Gaussian mixture, a uniform, etc., to construct 4 toy datasets. Each dataset contains 900 signals for training and 100 signals for test. The MNIST dataset consists of 60000 training samples and 10000 test samples with size 28×28 . We use six loss functions including the \mathcal{L}_{MC} [42], the original-domain consistency (OC) loss $\mathcal{L}_{OC} = \|\hat{\mathbf{x}} - \mathcal{F}_\Theta(\mathbf{A}\hat{\mathbf{x}}, \mathbf{A}, \gamma)\|_p^p$ [57], our \mathcal{L}_{DMC} and \mathcal{L}_{DOC} , the supervised loss $\mathcal{L}_{sup} = \|\mathbf{x} - \mathcal{F}_\Theta(\mathbf{A}\mathbf{x}, \mathbf{A}, \gamma)\|_p^p$, and their various combinations to train six SC-CNNs with $K = 3$, $C = 16$, and without the final GD step for 30000 epochs. The measurements $\{\mathbf{y}_i\}$ are generated by a fixed Gaussian matrix of ratio 50% from GTs.

³Please refer to Sec. B in the [supplementary material](#) for more experimental details, results, and analyses.

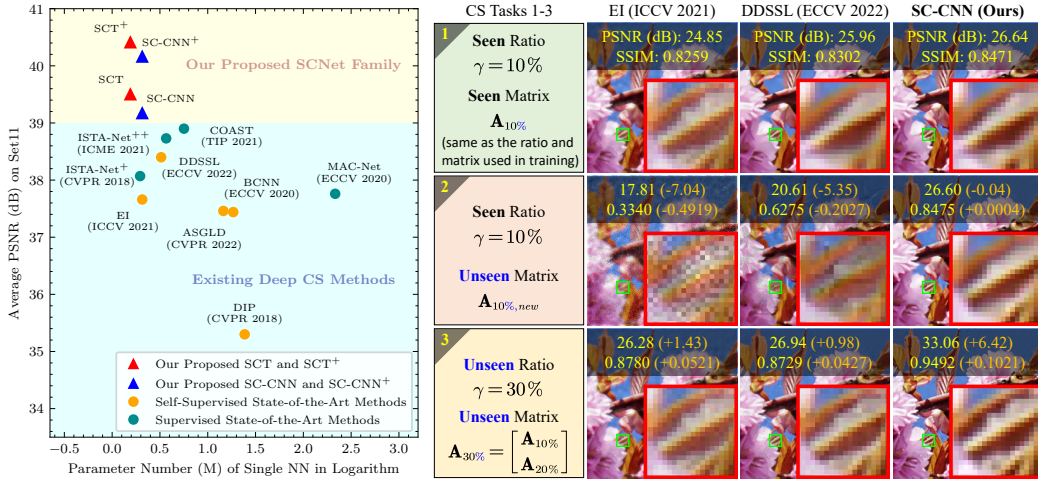


Figure 4: (Left) Comparison of PSNR and parameter number among our SCNets and nine existing methods with $\gamma = 50\%$ and $\sigma = 0$. (Right) The reconstructions of an image named “0898” from DIV2K [122] produced by three self-supervised methods: EI [57], DDSSL [40], and our SC-CNN with only external learning (*i.e.*, stage-1). (The 1st row) NNs are first tested in the setting of ratio 10% and a matrix consistent with the ones adopted during training. (The 2nd and 3rd rows) They are then extended to new ratios and matrices that were not provided or seen in the training set (marked as “Unseen”). Our SC-CNN keeps robust to different settings once trained (with all matrices being Gaussian and satisfying $\mathbf{A}\mathbf{A}^\top = \mathbf{I}$), while EI and DDSSL may fail and be sensitive to task changes.

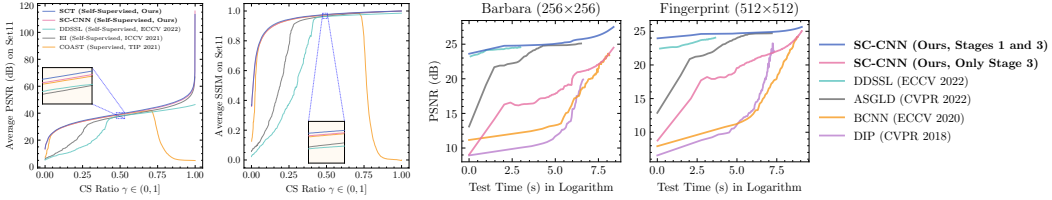


Figure 5: (Left) Comparison of ratio-scalability among five CS NNs. The four self-supervised NNs are trained on a measurement set of ratio 50%. The supervised COAST [29] is trained on five ratios: 10%, 20%, 30%, 40%, and 50%. SCNets generalize well to the entire range $(0, 1]$ once trained, with significant performance leading over others sensitive to ratio changes. (Right) Comparison of six NNs that use test-time single-image internal learning (*i.e.*, stage-3) on two images from Set11 [22]. DIP [42], BCNN [44], ASGLD [63], and SC-CNN (only stage-3) are trained from scratch. DDSSL [40] and SC-CNN (stages 1 and 3) are initialized by the NN weights from their offline external learning.

Results. Fig. 3 reports the comparison on reconstruction accuracy among $\mathbf{A}^\dagger \mathbf{y}$ and SC-CNNs trained by the six losses. We observe that: (1) “MC” and “MC+OC” may overfit to undesirable results. This can be alleviated by our measurement divisions in “DMC”, which exhibits steady and continuous growth in test accuracy; (2) our DOC encouragement brings significant performance improvements (SNR > 10 dB on toy signals and PSNR > 1.8 dB on MNIST), and makes “DMC+DOC” competitive to the supervised counterpart, with distances < 2.5 dB. In Fig. 3 (bottom-left), we visualize the learning trajectories of NN weights for different methods. Remarkably, our DMC and DOC encouragements can guide the NNs to learn the common knowledge and signal priors among various CS tasks: the NN weights optimized with our \mathcal{L}_{DMC} and \mathcal{L}_{DOC} present an obvious convergence tendency towards the weight cluster trained by \mathcal{L}_{sup} across different sampling ratios, effectively avoiding trivial solutions.

3.2 CS Reconstruction for Natural Images

Setup. We simulate $\mathbf{y} = \mathbf{A}\mathbf{x} + \mathbf{n}$ on 88912 randomly cropped image blocks of size $N = 33 \times 33$ [87] from T91 [123, 22] to create a measurement set $\{\mathbf{y}_i^{train}\}$ using a fixed block-based (or block-diagonal) [124, 125] Gaussian matrix \mathbf{A} for external learning. Six *supervised* methods: ReconNet [22], ISTA-Net⁺ [87], DPA-Net [26], MAC-Net [25], ISTA-Net⁺⁺ [27], and COAST [29], and six *self-supervised* approaches: DIP [42], BCNN [44], EI [57], REI [58], ASGLD [63], and DDSSL [40] are incorporated for comparison. Following [40], we implement EI by applying the EI loss to SC-CNN when $\sigma = 0$, and replace it with its enhanced robust version REI when $\sigma > 0$. For SCNets, we set $K = 20$ and $C = 32$ by default⁴. Four benchmarks: Set11 [22], CBSD68 [120], Urban100

⁴For reproducible research, the source code of our SCNets with pre-trained weights will be made available.

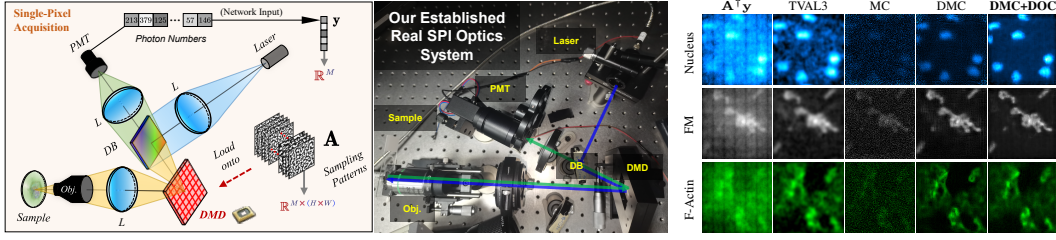


Figure 6: (Left) Illustration of our SPI system. A set of optical instruments and DMD modulation patterns are used to implement $y = Ax$. (Middle) Layout of our SPI system on testbed. Blue arrows represent emission path of light from laser to sample, while green arrows correspond to excitation path of fluorescence from sample to PMT. Obj.: objective; L: lens; DMD: digital micro-mirror device; DB: dichroic beamsplitter; PMT: photomultiplier. (Right) Visual comparison among five methods. We provide the 1st 2D slice for 3D reconstruction of F-actin. Our method yields best SPI qualities.

[121], and DIV2K [122] are employed. Test images from Urban100 and DIV2K are all 256×256 center-cropped. Results are evaluated by PSNR and SSIM [126] on the Y channel in YCrCb space.

Results. Tab. 1 and Fig. 4 (left) provide comparisons among different methods. We observe that: (1) the standard SCNets are competitive with both existing best supervised and self-supervised methods (e.g., COAST [29] and DDSSL [40]), especially when $\gamma > 10\%$, while enjoying low parameter cost ($< 0.4M$) and real-time inference speeds ($> 30fps$); (2) our internal learning and self-ensemble schemes in stages 2-4 of SC-CNN⁺ and SCT⁺ bring PSNR improvements of 0.18-3.98dB with a negligible additional parameter burden for single NN, demonstrating the effectiveness of our loss \mathcal{L} and progressive reconstruction strategy. Figs. 4 (right) and 5 (left) reveal the remarkable generalization ability of SCNets on the entire ratio range $(0, 1]$ and arbitrary matrices once trained on an incomplete measurement set. In contrast, competing methods EI [57] and DDSSL [40] suffer from unexpected performance drops and yield suboptimal results when the ratio and matrix change due to requirement variations and hardware malfunctions. While these methods may struggle to adapt to such changeable settings in real-world deployments, our method not only achieves superior performance, but also exhibits favorable scalability and robustness given only fixed external measurements. In Fig. 5 (right), we observe that our SC-CNN is capable of providing recoveries by utilizing only the stage-3, with its NN capacity being much smaller than that of others, and can significantly benefit from the weight initialization of stage-1 training, demonstrating its flexibility for different real environments.

3.3 CS Reconstruction for Fluorescence Microscopy with Real SPI Optics System

Setup. To verify the effectiveness of our method in real CS scenarios, we establish an SPI [4, 22, 5] optics system for fluorescence microscopy [108]. The hardware setup is illustrated in Figs. 6 (left) and (middle). More details are provided by Sec. B.3 in [supplementary material](#). Our DMD sequences (in time) through $2M$ projections, implementing the $M = 5000$ rows of an $M \times N$ bipolar matrix A , where each projection appears as an $N = 128 \times 128$ pattern, and all matrix elements are i.i.d. Bernoulli and has an equal probability of 0.5 for being $+1/-1$. We use three types of samples: nucleus, fluorescent microsphere (FM), and filamentous actin (F-Actin). For the former two, we obtain 950/50 ys of size M for training/test. For F-actin, we capture 490/10 groups of training/test measurements. Each group contains 21 ys corresponding to 21 2D slices (xs) along the z-axis. We employ SC-CNN ($K = 20$, $C = 32$, and trained by only stage-1) without IE, PE, and final GD step. For 3D imaging of F-actin samples, we set $C = 64$ and concatenate the 21 slices channel-wise to recover them jointly.

Results. Fig. 6 (right) displays the reconstructed results of five methods at ratio $\gamma = 5000/16384 \approx 30.5\%$. We observe that: (1) $A^\dagger y$, TVAL3 [14], and “MC” [42] methods can reconstruct some basic structures, but may also introduce undesirable artifacts and the loss of some important image features; (2) our “DMC” can well suppress noise and yield better results, while “DMC+DOC” can provide further improved preservation and balance of the primary features and details for all three sample types, producing enhanced and clearer informative nuclear speckles [127] and FM/F-actin intensities. These findings confirm the efficacy of our method for real data, its performance superiority, and better generalization ability than existing methods, once trained on a single collected measurement set of fixed ratio and matrix. It is worth noting that the imaging results can be further enhanced by adopting our default SCT⁺, equipped with the fully-activated four-stage reconstruction ($1 \rightarrow 2 \rightarrow 3 \rightarrow 4$).

4 Conclusions

We propose a novel self-supervised scalable CS method, consisting of an SCL scheme and an SCNet family. SCL employs a dual-domain loss to learn a general image-/ratio-/matrix-agnostic mapping

instead of specific ones from partial measurements by augmenting and encouraging random cross-consistency and arbitrary sampling-reconstruction cycle-consistency. A four-stage strategy further improves accuracy progressively. SCNet is designed based on PGD inspiration and well regularized by NN mechanisms. The combination and mutual promotion of SCL and SCNet effectively exploit available data and information to drive deep reconstruction toward valid results that can even surpass those predicted by supervised NNs. Experiments demonstrate the effectiveness and superiority of our method in achieving a better balance among imaging quality, flexibility, scalability, complexity, and interpretability than existing ones, thus paving the way for practical CS imaging applications. Our future work is to extend this method for other inverse imaging problems, including but not limited to inpainting, deconvolution [86], MRI [7, 8], CT [9], SCI [10], and interferometric imaging [37, 80].

References

- [1] David L Donoho. Compressed Sensing. *IEEE Transactions on Information Theory*, 52(4):1289–1306, 2006.
- [2] Emmanuel J Candès et al. Compressive Sampling. In *Proceedings of International Congress of Mathematicians (ICM)*, volume 3, pages 1433–1452, 2006.
- [3] Claude E Shannon. Communication in the Presence of Noise. *Proceedings of Institute of Radio Engineers (IRE)*, 37(1):10–21, 1949.
- [4] Marco F Duarte, Mark A Davenport, Dharmpal Takhar, Jason N Laska, Ting Sun, Kevin F Kelly, and Richard G Baraniuk. Single-Pixel Imaging via Compressive Sampling. *IEEE Signal Processing Magazine*, 25(2):83–91, 2008.
- [5] Weili Li, Xuemei Hu, Jingbo Wu, Kebin Fan, Benwen Chen, Caihong Zhang, Wei Hu, Xun Cao, Biaobing Jin, Yanqing Lu, et al. Dual-Color Terahertz Spatial Light Modulator for Single-Pixel Imaging. *Light: Science & Applications*, 11(1):1–10, 2022.
- [6] Antonio Lorente Mur, Françoise Peyrin, and Nicolas Ducros. Deep Expectation-Maximization for Single-Pixel Image Reconstruction With Signal-Dependent Noise. *IEEE Transactions on Computational Imaging*, 8:759–769, 2022.
- [7] Michael Lustig, David L Donoho, Juan M Santos, and John M Pauly. Compressed Sensing MRI. *IEEE Signal Processing Magazine*, 25(2):72–82, 2008.
- [8] Jian Sun, Huibin Li, Zongben Xu, et al. Deep ADMM-Net for Compressive Sensing MRI. In *Proceedings of Neural Information Processing Systems (NeurIPS)*, volume 29, pages 10–18, 2016.
- [9] Timothy P Szczykutowicz and Guang-Hong Chen. Dual Energy CT Using Slow kVp Switching Acquisition and Prior Image Constrained Compressed Sensing. *Physics in Medicine & Biology*, 55(21):6411, 2010.
- [10] Ying Fu, Tao Zhang, Lizhi Wang, and Hua Huang. Coded Hyperspectral Image Reconstruction Using Deep External and Internal Learning. *IEEE Transactions on Pattern Analysis and Machine Intelligence*, 44(7):3404–3420, 2021.
- [11] Xuanyu Zhang, Bin Chen, Wenzhen Zou, Shuai Liu, Yongbing Zhang, Ruiqin Xiong, and Jian Zhang. Progressive Content-aware Coded Hyperspectral Compressive Imaging. *arXiv preprint arXiv:2303.09773*, 2023.
- [12] Michal Aharon, Michael Elad, and Alfred Bruckstein. K-SVD: An Algorithm for Designing Overcomplete Dictionaries for Sparse Representation. *IEEE Transactions on Signal Processing*, 54(11):4311–4322, 2006.
- [13] Sivan Gleichman and Yonina C Eldar. Blind compressed sensing. *IEEE Transactions on Information Theory*, 57(10):6958–6975, 2011.
- [14] Chengbo Li, Wotao Yin, Hong Jiang, and Yin Zhang. An Efficient Augmented Lagrangian Method with Applications to Total Variation Minimization. *Computational Optimization and Applications*, 56(3):507–530, 2013.

- [15] Emmanuel Candes and Benjamin Recht. Exact matrix completion via convex optimization. *Communications of the ACM*, 55(6):111–119, 2012.
- [16] Jian Zhang, Debin Zhao, and Wen Gao. Group-based Sparse Representation for Image Restoration. *IEEE Transactions on Image Processing*, 23(8):3336–3351, 2014.
- [17] Weisheng Dong, Guangming Shi, Xin Li, Yi Ma, and Feng Huang. Compressive Sensing via Nonlocal Low-Rank Regularization. *IEEE Transactions on Image Processing*, 23(8):3618–3632, 2014.
- [18] Jian-Feng Cai, Hui Ji, Zuowei Shen, and Gui-Bo Ye. Data-driven Tight Frame Construction and Image Denoising. *Applied and Computational Harmonic Analysis*, 37(1):89–105, 2014.
- [19] Mohammad Aghagolzadeh and Hayder Radha. New guarantees for blind compressed sensing. In *Proceedings of IEEE Allerton Conference on Communication, Control, and Computing*, pages 1227–1234, 2015.
- [20] Il Yong Chun and Jeffrey A Fessler. Convolutional Analysis Operator Learning: Acceleration and Convergence. *IEEE Transactions on Image Processing*, 29:2108–2122, 2019.
- [21] Ali Mousavi, Ankit B Patel, and Richard G Baraniuk. A Deep Learning Approach to Structured Signal Recovery. In *Proceedings of IEEE Allerton Conference on Communication, Control, and Computing*, pages 1336–1343, 2015.
- [22] Kuldeep Kulkarni, Suhas Lohit, Pavan Turaga, Ronan Kerviche, and Amit Ashok. ReconNet: Non-iterative Reconstruction of Images from Compressively Sensed Measurements. In *Proceedings of IEEE Conference on Computer Vision and Pattern Recognition (CVPR)*, pages 449–458, 2016.
- [23] Davis Gilton, Greg Ongie, and Rebecca Willett. Neumann Networks for Linear Inverse Problems in Imaging. *IEEE Transactions on Computational Imaging*, 6:328–343, 2019.
- [24] Wuzhen Shi, Feng Jiang, Shaohui Liu, and Debin Zhao. Scalable Convolutional Neural Network for Image Compressed Sensing. In *Proceedings of IEEE Conference on Computer Vision and Pattern Recognition (CVPR)*, pages 12290–12299, 2019.
- [25] Jiwei Chen, Yubao Sun, Qingshan Liu, and Rui Huang. Learning Memory Augmented Cascading Network for Compressed Sensing of Images. In *Proceedings of European Conference on Computer Vision (ECCV)*, pages 513–529, 2020.
- [26] Yubao Sun, Jiwei Chen, Qingshan Liu, Bo Liu, and Guodong Guo. Dual-Path Attention Network for Compressed Sensing Image Reconstruction. *IEEE Transactions on Image Processing*, 29:9482–9495, 2020.
- [27] Di You, Jingfen Xie, and Jian Zhang. ISTA-Net⁺⁺: Flexible Deep Unfolding Network for Compressive Sensing. In *Proceedings of IEEE International Conference on Multimedia and Expo (ICME)*, pages 1–6, 2021.
- [28] Davis Gilton, Gregory Ongie, and Rebecca Willett. Deep Equilibrium Architectures for Inverse Problems in Imaging. *IEEE Transactions on Computational Imaging*, 7:1123–1133, 2021.
- [29] Di You, Jian Zhang, Jingfen Xie, Bin Chen, and Siwei Ma. COAST: COntrollable Arbitrary-Sampling NeTwork for Compressive Sensing. *IEEE Transactions on Image Processing*, 30:6066–6080, 2021.
- [30] Zhonghao Zhang, Yipeng Liu, Jiani Liu, Fei Wen, and Ce Zhu. AMP-Net: Denoising-based Deep Unfolding for Compressive Image Sensing. *IEEE Transactions on Image Processing*, 30:1487–1500, 2021.
- [31] Bin Chen and Jian Zhang. Content-aware Scalable Deep Compressed Sensing. *IEEE Transactions on Image Processing*, 31:5412–5426, 2022.
- [32] Wenjun Chen, Chunling Yang, and Xin Yang. FSOINet: Feature-Space Optimization-Inspired Network for Image Compressive Sensing. In *Proceedings of IEEE International Conference on Acoustics, Speech and Signal Processing (ICASSP)*, pages 2460–2464, 2022.

- [33] Weiqi Li, Bin Chen, and Jian Zhang. D3C2-Net: Dual-Domain Deep Convolutional Coding Network for Compressive Sensing. *arXiv preprint arXiv:2207.13560*, 2022.
- [34] Tao Zhang, Ying Fu, Debing Zhang, and Chun Hu. Deep external and internal learning for noisy compressive sensing. *Neurocomputing*, 531:61–73, 2023.
- [35] Fei Wang, Chenglong Wang, Mingliang Chen, Wenlin Gong, Yu Zhang, Shensheng Han, and Guohai Situ. Far-field super-resolution ghost imaging with a deep neural network constraint. *Light: Science & Applications*, 11(1):1, 2022.
- [36] Daixuan Wu, Jiawei Luo, Guoqiang Huang, Yuanhua Feng, Xiaohua Feng, Runsen Zhang, Yuecheng Shen, and Zhaohui Li. Imaging biological tissue with high-throughput single-pixel compressive holography. *Nature Communications*, 12(1):4712, 2021.
- [37] He Sun and Katherine L Bouman. Deep probabilistic imaging: Uncertainty quantification and multi-modal solution characterization for computational imaging. In *Proceedings of the AAAI Conference on Artificial Intelligence*, pages 2628–2637, 2021.
- [38] Meng Lyu, Wei Wang, Hao Wang, Haichao Wang, Guowei Li, Ni Chen, and Guohai Situ. Deep-learning-based ghost imaging. *Scientific Reports*, 7(1):17865, 2017.
- [39] Catherine F Higham, Roderick Murray-Smith, Miles J Padgett, and Matthew P Edgar. Deep learning for real-time single-pixel video. *Scientific Reports*, 8(1):2369, 2018.
- [40] Yuhui Quan, Xinran Qin, Tongyao Pang, and Hui Ji. Dual-Domain Self-Supervised Learning and Model Adaption for Deep Compressive Imaging. In *Proceedings of European Conference on Computer Vision (ECCV)*, pages 409–426, 2022.
- [41] Adnan Qayyum, Inaam Ilahi, Fahad Shamshad, Farid Boussaid, Mohammed Bennamoun, and Junaid Qadir. Untrained neural network priors for inverse imaging problems: A survey. *IEEE Transactions on Pattern Analysis and Machine Intelligence*, 2022.
- [42] Dmitry Ulyanov, Andrea Vedaldi, and Victor Lempitsky. Deep Image Prior. In *Proceedings of IEEE Conference on Computer Vision and Pattern Recognition (CVPR)*, pages 9446–9454, 2018.
- [43] Reinhard Heckel and Mahdi Soltanolkotabi. Compressive sensing with un-trained neural networks: Gradient descent finds a smooth approximation. In *Proceedings of International Conference on Learning Representations (ICLR)*, pages 4149–4158, 2020.
- [44] Tongyao Pang, Yuhui Quan, and Hui Ji. Self-Supervised Bayesian Deep Learning for Image Recovery with Applications to Compressive Sensing. In *Proceedings of European Conference on Computer Vision (ECCV)*, pages 475–491, 2020.
- [45] Yuhui Quan, Mingqin Chen, Tongyao Pang, and Hui Ji. Self2Self With Dropout: Learning Self-Supervised Denoising From Single Image. In *Proceedings of IEEE Conference on Computer Vision and Pattern Recognition (CVPR)*, pages 1890–1898, 2020.
- [46] Jaakko Lehtinen, Jacob Munkberg, Jon Hasselgren, Samuli Laine, Tero Karras, Miika Aittala, and Timo Aila. Noise2Noise: Learning image restoration without clean data. In *Proceedings of International Conference on Machine Learning (ICML)*, 2018.
- [47] Charles M Stein. Estimation of the mean of a multivariate normal distribution. *The Annals of Statistics*, pages 1135–1151, 1981.
- [48] Yonina C Eldar. Generalized SURE for exponential families: Applications to regularization. *IEEE Transactions on Signal Processing*, 57(2):471–481, 2008.
- [49] Shakarim Soltanayev and Se Young Chun. Training deep learning based denoisers without ground truth data. In *Proceedings of Neural Information Processing Systems (NeurIPS)*, volume 31, 2018.
- [50] Magauyiya Zhussip, Shakarim Soltanayev, and Se Young Chun. Extending Stein’s unbiased risk estimator to train deep denoisers with correlated pairs of noisy images. In *Proceedings of Neural Information Processing Systems (NeurIPS)*, volume 32, 2019.

- [51] Zhihao Xia and Ayan Chakrabarti. Training image estimators without image ground truth. In *Proceedings of Neural Information Processing Systems (NeurIPS)*, volume 32, 2019.
- [52] Burhaneddin Yaman, Seyed Amir Hossein Hosseini, Steen Moeller, Jutta Ellermann, Kâmil Uğurbil, and Mehmet Akçakaya. Self-supervised learning of physics-guided reconstruction neural networks without fully sampled reference data. *Magnetic Resonance in Medicine*, 84(6):3172–3191, 2020.
- [53] Jiaming Liu, Yu Sun, Cihat Eldeniz, Weijie Gan, Hongyu An, and Ulugbek S Kamilov. RARE: Image reconstruction using deep priors learned without groundtruth. *IEEE Journal of Selected Topics in Signal Processing*, 14(6):1088–1099, 2020.
- [54] Christopher A Metzler, Ali Mousavi, Reinhard Heckel, and Richard G Baraniuk. Unsupervised learning with Stein’s unbiased risk estimator. *arXiv preprint arXiv:1805.10531*, 2018.
- [55] Magauiya Zhussip, Shakarim Soltanayev, and Se Young Chun. Training deep learning based image denoisers from undersampled measurements without ground truth and without image prior. In *Proceedings of IEEE Conference on Computer Vision and Pattern Recognition (CVPR)*, pages 10255–10264, 2019.
- [56] Chris Metzler, Ali Mousavi, and Richard Baraniuk. Learned D-AMP: Principled Neural Network based Compressive Image Recovery. In *Proceedings of Neural Information Processing Systems (NeurIPS)*, volume 30, 2017.
- [57] Dongdong Chen, Julián Tachella, and Mike E Davies. Equivariant Imaging: Learning Beyond the Range Space. In *Proceedings of IEEE International Conference on Computer Vision (ICCV)*, pages 4379–4388, 2021.
- [58] Dongdong Chen, Julián Tachella, and Mike E Davies. Robust Equivariant Imaging: a Fully Unsupervised Framework for Learning to Image from Noisy and Partial Measurements. In *Proceedings of IEEE Conference on Computer Vision and Pattern Recognition (CVPR)*, pages 5647–5656, 2022.
- [59] Dongdong Chen, Mike Davies, Matthias J Ehrhardt, Carola-Bibiane Schönlieb, Ferdia Sherry, and Julián Tachella. Imaging With Equivariant Deep Learning: From unrolled network design to fully unsupervised learning. *IEEE Signal Processing Magazine*, 40(1):134–147, 2023.
- [60] Julián Tachella, Dongdong Chen, and Mike Davies. Unsupervised Learning From Incomplete Measurements for Inverse Problems. In *Proceedings of Neural Information Processing Systems (NeurIPS)*, 2022.
- [61] Julián Tachella, Dongdong Chen, and Mike Davies. Sensing theorems for unsupervised learning in linear inverse problems. *Journal of Machine Learning Research*, 24(39):1–45, 2022.
- [62] Tongyao Pang, Huan Zheng, Yuhui Quan, and Hui Ji. Recorrupted-to-recorrupted: unsupervised deep learning for image denoising. In *Proceedings of IEEE Conference on Computer Vision and Pattern Recognition (CVPR)*, pages 2043–2052, 2021.
- [63] Weixi Wang, Ji Li, and Hui Ji. Self-supervised Deep Image Restoration via Adaptive Stochastic Gradient Langevin Dynamics. In *Proceedings of IEEE Conference on Computer Vision and Pattern Recognition (CVPR)*, pages 1989–1998, 2022.
- [64] Ashish Bora, Ajil Jalal, Eric Price, and Alexandros G Dimakis. Compressed sensing using generative models. In *Proceedings of International Conference on Machine Learning (ICML)*, pages 537–546, 2017.
- [65] Ashish Bora, Eric Price, and Alexandros G Dimakis. AmbientGAN: Generative models from lossy measurements. In *Proceedings of International Conference on Learning Representations (ICLR)*, 2018.
- [66] Maya Kabkab, Pouya Samangouei, and Rama Chellappa. Task-aware compressed sensing with generative adversarial networks. In *Proceedings of the AAAI Conference on Artificial Intelligence*, 2018.

- [67] Yan Wu, Mihaela Rosca, and Timothy Lillicrap. Deep compressed sensing. In *Proceedings of International Conference on Machine Learning (ICML)*, pages 6850–6860, 2019.
- [68] Ankit Raj, Yuqi Li, and Yoram Bresler. GAN-based projector for faster recovery with convergence guarantees in linear inverse problems. In *Proceedings of IEEE Conference on Computer Vision and Pattern Recognition (CVPR)*, pages 5602–5611, 2019.
- [69] Wei Wang, Fei Wen, Zeyu Yan, and Peilin Liu. Optimal transport for unsupervised denoising learning. *IEEE Transactions on Pattern Analysis and Machine Intelligence*, 2022.
- [70] Singanallur V Venkatakrishnan, Charles A Bouman, and Brendt Wohlberg. Plug-and-play priors for model based reconstruction. In *Proceedings of IEEE Global Conference on Signal and Information Processing*, pages 945–948, 2013.
- [71] Yu Sun, Brendt Wohlberg, and Ulugbek S Kamilov. An Online Plug-and-Play Algorithm for Regularized Image Reconstruction. *IEEE Transactions on Computational Imaging*, 5(3):395–408, 2019.
- [72] Ernest Ryu, Jialin Liu, Sicheng Wang, Xiaohan Chen, Zhangyang Wang, and Wotao Yin. Plug-and-Play Methods Provably Converge with Properly Trained Denoisers. In *Proceedings of International Conference on Machine Learning (ICML)*, pages 5546–5557, 2019.
- [73] Zahra Kadkhodaie and Eero Simoncelli. Stochastic solutions for linear inverse problems using the prior implicit in a denoiser. In *Proceedings of Neural Information Processing Systems (NeurIPS)*, volume 34, pages 13242–13254, 2021.
- [74] Ulugbek S Kamilov, Charles A Bouman, Gregory T Buzzard, and Brendt Wohlberg. Plug-and-Play Methods for Integrating Physical and Learned Models in Computational Imaging: Theory, algorithms, and applications. *IEEE Signal Processing Magazine*, 40(1):85–97, 2023.
- [75] Yaniv Romano, Michael Elad, and Peyman Milanfar. The little engine that could: Regularization by denoising (RED). *SIAM Journal on Imaging Sciences*, 10(4):1804–1844, 2017.
- [76] Jiaming Liu, Xiaojian Xu, Weijie Gan, Ulugbek Kamilov, et al. Online deep equilibrium learning for regularization by denoising. In *Proceedings of Neural Information Processing Systems (NeurIPS)*, volume 35, pages 25363–25376, 2022.
- [77] Bahjat Kawar, Michael Elad, Stefano Ermon, and Jiaming Song. Denoising diffusion restoration models. In *Proceedings of Neural Information Processing Systems (NeurIPS)*, 2022.
- [78] Yinhuai Wang, Jiwen Yu, and Jian Zhang. Zero-Shot Image Restoration Using Denoising Diffusion Null-Space Model. In *Proceedings of International Conference on Learning Representations (ICLR)*, 2023.
- [79] Hyungjin Chung, Jeongsol Kim, Michael T Mccann, Marc L Klasky, and Jong Chul Ye. Diffusion posterior sampling for general noisy inverse problems. In *Proceedings of International Conference on Learning Representations (ICLR)*, 2023.
- [80] Berthy T Feng, Jamie Smith, Michael Rubinstein, Huiwen Chang, Katherine L Bouman, and William T Freeman. Score-based diffusion models as principled priors for inverse imaging. *arXiv preprint arXiv:2304.11751*, 2023.
- [81] Kai Zhang, Yawei Li, Wangmeng Zuo, Lei Zhang, Luc Van Gool, and Radu Timofte. Plug-and-Play Image Restoration with Deep Denoiser Prior. *IEEE Transactions on Pattern Analysis and Machine Intelligence*, 44(10):6360–6376, 2022.
- [82] Renhao Liu, Yu Sun, Jiabei Zhu, Lei Tian, and Ulugbek S Kamilov. Recovery of continuous 3D refractive index maps from discrete intensity-only measurements using neural fields. *Nature Machine Intelligence*, 4(9):781–791, 2022.
- [83] David L Donoho, Arian Maleki, and Andrea Montanari. Message-Passing Algorithms for Compressed Sensing. *Proceedings of the National Academy of Sciences*, 106(45):18914–18919, 2009.

- [84] Gesen Zhang, Shuhong Jiao, Xiaoli Xu, and Lan Wang. Compressed sensing and reconstruction with Bernoulli matrices. In *Proceedings of IEEE International Conference on Information and Automation (ICIA)*, pages 455–460, 2010.
- [85] Chen Zhao, Siwei Ma, Jian Zhang, Ruiqin Xiong, and Wen Gao. Video Compressive Sensing Reconstruction via Reweighted Residual Sparsity. *IEEE Transactions on Circuits and Systems for Video Technology*, 27(6):1182–1195, 2016.
- [86] Yuhui Quan, Zhuojie Chen, Huan Zheng, and Hui Ji. Learning deep non-blind image deconvolution without ground truths. In *Proceedings of European Conference on Computer Vision (ECCV)*, pages 642–659, 2022.
- [87] Jian Zhang and Bernard Ghanem. ISTA-Net: Interpretable Optimization-Inspired Deep Network for Image Compressive Sensing. In *Proceedings of IEEE Conference on Computer Vision and Pattern Recognition (CVPR)*, pages 1828–1837, 2018.
- [88] Yinbo Chen, Sifei Liu, and Xiaolong Wang. Learning continuous image representation with local implicit image function. In *Proceedings of IEEE Conference on Computer Vision and Pattern Recognition (CVPR)*, pages 8628–8638, 2021.
- [89] Jaewon Lee and Kyong Hwan Jin. Local texture estimator for implicit representation function. In *Proceedings of IEEE Conference on Computer Vision and Pattern Recognition (CVPR)*, pages 1929–1938, 2022.
- [90] Jiabao Li, Yuqi Li, Chong Wang, Xulun Ye, and Wolfgang Heidrich. BUSIFusion: Blind Unsupervised Single Image Fusion of Hyperspectral and RGB Images. *IEEE Transactions on Computational Imaging*, 9:94–105, 2023.
- [91] Karol Gregor and Yann LeCun. Learning Fast Approximations of Sparse Coding. In *Proceedings of International Conference on Machine Learning (ICML)*, pages 399–406, 2010.
- [92] Vishal Monga, Yuelong Li, and Yonina C Eldar. Algorithm Unrolling: Interpretable, Efficient Deep Learning for Signal and Image Processing. *IEEE Signal Processing Magazine*, 38(2):18–44, 2021.
- [93] Jian Zhang, Bin Chen, Ruiqin Xiong, and Yongbing Zhang. Physics-Inspired Compressive Sensing: Beyond deep unrolling. *IEEE Signal Processing Magazine*, 40(1):58–72, 2023.
- [94] Qian Ning, Weisheng Dong, Guangming Shi, Leida Li, and Xin Li. Accurate and lightweight image super-resolution with model-guided deep unfolding network. *IEEE Journal of Selected Topics in Signal Processing*, 15(2):240–252, 2020.
- [95] Jiechong Song, Bin Chen, and Jian Zhang. Deep Memory-Augmented Proximal Unrolling Network for Compressive Sensing. *International Journal of Computer Vision*, pages 1–20, 2023.
- [96] Wenxue Cui, Shaohui Liu, and Debin Zhao. Fast Hierarchical Deep Unfolding Network for Image Compressed Sensing. In *Proceedings of ACM International Conference on Multimedia (ACM MM)*, pages 2739–2748, 2022.
- [97] Jiechong Song, Bin Chen, and Jian Zhang. Dynamic Path-Controllable Deep Unfolding Network for Compressive Sensing. *IEEE Transactions on Image Processing*, 2023.
- [98] Chengbo Li, Hong Jiang, Paul Wilford, Yin Zhang, and Mike Scheutzw. A new compressive video sensing framework for mobile broadcast. *IEEE Transactions on Broadcasting*, 59(1):197–205, 2013.
- [99] Wenbin Yin, Xiaopeng Fan, Yunhui Shi, Ruiqin Xiong, and Debin Zhao. Compressive sensing based soft video broadcast using spatial and temporal sparsity. *Mobile Networks and Applications*, 21:1002–1012, 2016.
- [100] Jill M Boyce, Yan Ye, Jianle Chen, and Adarsh K Ramasubramanian. Overview of SHVC: Scalable extensions of the high efficiency video coding standard. *IEEE Transactions on Circuits and Systems for Video Technology*, 26(1):20–34, 2015.

- [101] Yuanhong Zhong, Chenxu Zhang, Fan Ren, Honggang Kuang, and Panliang Tang. Scalable image compressed sensing with generator networks. *IEEE Transactions on Computational Imaging*, 8:1025–1037, 2022.
- [102] Kai Zhang, Wangmeng Zuo, and Lei Zhang. FFDNet: Toward a Fast and Flexible Solution for CNN-based Image Denoising. *IEEE Transactions on Image Processing*, 27(9):4608–4622, 2018.
- [103] Jingwen He, Chao Dong, and Yu Qiao. Modulating image restoration with continual levels via adaptive feature modification layers. In *Proceedings of IEEE Conference on Computer Vision and Pattern Recognition (CVPR)*, pages 11056–11064, 2019.
- [104] Jingwen He, Chao Dong, and Yu Qiao. Interactive multi-dimension modulation with dynamic controllable residual learning for image restoration. In *Proceedings of European Conference on Computer Vision (ECCV)*, pages 53–68, 2020.
- [105] Haoming Cai, Jingwen He, Yu Qiao, and Chao Dong. Toward interactive modulation for photo-realistic image restoration. In *Proceedings of IEEE Conference on Computer Vision and Pattern Recognition Workshops (CVPRW)*, pages 294–303, 2021.
- [106] Chong Mou, Yanze Wu, Xintao Wang, Chao Dong, Jian Zhang, and Ying Shan. Metric learning based interactive modulation for real-world super-resolution. In *Proceedings of European Conference on Computer Vision (ECCV)*, pages 723–740, 2022.
- [107] Neal Parikh, Stephen Boyd, et al. Proximal Algorithms. *Foundations and in Optimization*, 1(3):127–239, 2014.
- [108] Jeff W Lichtman and José-Angel Conchello. Fluorescence microscopy. *Nature Methods*, 2(12):910–919, 2005.
- [109] David L Donoho, Xiaoming Huo, et al. Uncertainty principles and ideal atomic decomposition. *IEEE Transactions on Information Theory*, 47(7):2845–2862, 2001.
- [110] Emmanuel J Candes and Terence Tao. Decoding by Linear Programming. *IEEE Transactions on Information Theory*, 51(12):4203–4215, 2005.
- [111] Emmanuel J Candes. The restricted isometry property and its implications for compressed sensing. *Comptes rendus mathématique*, 346(9-10):589–592, 2008.
- [112] Hamid Nouasria and Mohamed Et-tolba. New constructions of Bernoulli and Gaussian sensing matrices for compressive sensing. In *Proceedings of IEEE International Conference on Wireless Networks and Mobile Communications (WINCOM)*, pages 1–5, 2017.
- [113] Yarin Gal and Zoubin Ghahramani. Dropout as a Bayesian approximation: Representing model uncertainty in deep learning. In *Proceedings of International Conference on Machine Learning (ICML)*, pages 1050–1059, 2016.
- [114] Kaiming He, Xiangyu Zhang, Shaoqing Ren, and Jian Sun. Deep Residual Learning for Image Recognition. In *Proceedings of IEEE Conference on Computer Vision and Pattern Recognition (CVPR)*, pages 770–778, 2016.
- [115] Kai Zhang, Yawei Li, Jingyun Liang, Jiezhang Cao, Yulun Zhang, Hao Tang, Radu Timofte, and Luc Van Gool. Practical Blind Denoising via Swin-Conv-UNet and Data Synthesis. *arXiv preprint arXiv:2203.13278*, 2022.
- [116] Dongdong Chen and Mike E Davies. Deep Decomposition Learning for Inverse Imaging Problems. In *Proceedings of European Conference on Computer Vision (ECCV)*, pages 510–526, 2020.
- [117] Kai Zhang, Wangmeng Zuo, Yunjin Chen, Deyu Meng, and Lei Zhang. Beyond a Gaussian Denoiser: Residual Learning of Deep CNN for Image Denoising. *IEEE Transactions on Image Processing*, 26(7):3142–3155, 2017.
- [118] Li Deng. The MNIST database of handwritten digit images for machine learning research. *IEEE Signal Processing Magazine*, 29(6):141–142, 2012.

- [119] Karl Pearson. On lines and planes of closest fit to systems of points in space. *The London, Edinburgh, and Dublin Philosophical Magazine and Journal of Science*, 2(11):559–572, 1901.
- [120] David Martin, Charless Fowlkes, Doron Tal, and Jitendra Malik. A Database of Human Segmented Natural Images and Its Application to Evaluating Segmentation Algorithms and Measuring Ecological Statistics. In *Proceedings of IEEE International Conference on Computer Vision (ICCV)*, volume 2, pages 416–423, 2001.
- [121] Jia-Bin Huang, Abhishek Singh, and Narendra Ahuja. Single Image Super-Resolution from Transformed Self-Exemplars. In *Proceedings of IEEE Conference on Computer Vision and Pattern Recognition (CVPR)*, pages 5197–5206, 2015.
- [122] Eirikur Agustsson and Radu Timofte. NTIRE 2017 Challenge on Single Image Super-Resolution: Dataset and Study. In *Proceedings of IEEE Conference on Computer Vision and Pattern Recognition Workshops (CVPRW)*, pages 126–135, 2017.
- [123] Chao Dong, Chen Change Loy, Kaiming He, and Xiaoou Tang. Learning a Deep Convolutional Network for Image Super-Resolution. In *Proceedings of European Conference on Computer Vision (ECCV)*, pages 184–199, 2014.
- [124] Lu Gan. Block Compressed Sensing of Natural Images. In *Proceedings of IEEE International Conference on Digital Signal Processing (ICDSP)*, pages 403–406, 2007.
- [125] Il Yong Chun and Ben Adcock. Compressed sensing and parallel acquisition. *IEEE Transactions on Information Theory*, 63(8):4860–4882, 2017.
- [126] Zhou Wang, Alan C Bovik, Hamid R Sheikh, and Eero P Simoncelli. Image Quality Assessment: From Error Visibility to Structural Similarity. *IEEE Transactions on Image Processing*, 13(4):600–612, 2004.
- [127] Katherine A Alexander, Allison Coté, Son C Nguyen, Liguozhang, Omid Gholamalamdari, Paula Agudelo-Garcia, Enrique Lin-Shiao, KMA Tanim, Joan Lim, Nicolas Biddle, et al. p53 mediates target gene association with nuclear speckles for amplified RNA expression. *Molecular Cell*, 81(8):1666–1681, 2021.